Fluorinated Reduced Graphene Oxide as an Interlayer in Li-S Batteries

A. Vizintin, M. Lozinšek, R.K. Chellappan, Dominique Foix, A. Krajnc, G. Mali, G. Drazic, B. Genorio, Rémi Dedryvère, R. Dominko

Fluorinated Reduced Graphene Oxide as an interlayer in Li-S batteries

Alen Vizintin[a,b], Matic Lozinsek[c], Rajesh Kumar Chellappan[d], Dominique Foix[d,e], Andraz Krajnc[a], Gregor Mali[a], Goran Drazic[a], Bostjan Genorio[b], Rémi Dedryvère[d,e], Robert Dominko[a,e]

[a] National Institute of Chemistry, Hajdrihova 19, 1000 Ljubljana, Slovenia
[b] University of Ljubljana, Faculty of Chemistry and Chemical Technology, Vecna pot 113, 1000 Ljubljana, Slovenia
[c] Jozef Stefan Institute, Jamova cesta 39, 1000 Ljubljana, Slovenia
[d] IPREM-ECP (UMR 5254 CNRS), University of Pau, Hélioparc, 2 av. Pierre Angot, 64053 Pau CEDEX 9, France
[e] Alistore - European Research Institute, 33 rue Saint-Leu, 80039 Amiens CEDEX, France

Abstract

We report on the synthesis of fluorinated reduced graphene oxide (F-rGO) by a direct fluorination of reduced graphene oxide (rGO) with XeF_2 or F_2/BF_3 in anhydrous HF. Characterization performed by HAADF-STEM and NMR confirmed the formation of C–F bonds, which is also supported by the color change from graphite grey to light yellow. F-rGO has been used as an interlayer additive supported by a glass fiber separator in lithium-sulfur (Li-S) batteries in order to block the diffusion/migration of polysulfides from the porous positive electrode to the metallic lithium electrode and to prevent the redox shuttle effect. Electrochemical cycling of Li-S batteries has confirmed the beneficial role of F-rGO separators, with a more pronounced effect observed for high degrees of fluorination. X-ray Photoelectron Spectroscopy (XPS) studies have shown a direct effect on the amount of Li_2S and polysulfides found on the lithium electrode, and evidenced a better reversibility of reduction/oxidation mechanisms of sulfur at the positive electrode upon discharge/charge.

Keywords

Lithium-sulfur batteries, hydrophobic interlayer, graphene oxide, fluorination, XPS, Li_2S

1. Introduction

The continuous demand for cheap batteries with higher energy density has pushed the alkali metal or alkali-earth metal anodes (Li, Na, Mg)[1–3] and sulfur based cathodes to the frontier of a battery research. Sulfur is cheap and sustainable cathode material. Used in combination with alkali metals constitutes a battery system which can be used in many different applications (from grid storage applications to battery driven cars).[4,5] Lithium anode and sulfur cathode is the most common system that has attracted researchers for several decades.[6,7]

Recent renewed interest in the lithium sulfur batteries was initiated by Nazar[8] due to increased demand of automotive industry for cheap, safe and sustainable batteries with high energy density. Since then it is a driving force for many research activities worldwide.[9,10] The majority of research activities in the field of Li-S batteries have been devoted to the development of a proper cathode host matrix, which can enable the full conversion of sulfur into Li_2S during the reduction process.[11,12] While proper structuring of the cathode host matrices can lead to the high conversion of sulfur to Li_2S, the morphology of the cathode composite is not capable of completely preventing the polysulfide diffusion out of the composite, primarily due to the high concentration gradient between electrodes. That can be at least partially improved by introducing sorption additives[13,14] in the cathode composite or by introducing double-coated cathodes. Both approaches improve capacity retention and stability; however, Coulombic efficiency is well below the level required for practical applications.

The need for the effective separation between the sulfur cathode and the lithium anode is in correlation with the reaction mechanism of Li-S batteries. Recent reports on the mechanism that was derived from different operando techniques[15–17] showed that the high voltage plateau at 2.4–2.3 V can be correlated to the reaction of sulfur with lithium to form long chain polysulfides which are highly soluble. The transition of voltage from 2.3 V to 2.1 V represents the conversion of long chain polysulfides to shorter polysulfides while the plateau at 2.1 V represents the precipitation of Li_2S. Since there are high concentrations of soluble polysulfides in the electrolyte during the beginning of discharge, it can be expected that sorption additives should be very efficient, particularly if high sulfur loading is present in the composite cathode. Another approach to prevent polysulfide diffusion and/or migration to the lithium anode is a selective barrier for polysulfides. Different types of carbon-based barriers have been recently introduced as an additional interlayer between the glass fiber or polyolefin separator and sulfur cathode. Interlayers composed of reduced graphene oxide (rGO) mixed

with an additional carbon black (CB)[18,19], conductive multi-walled carbon nanotube (MWCNT)[20] or microporous carbon paper[21] have an effect on the capacity stabilization. These additional barriers prevent the migration of lithium polysulfides towards the lithium side and have an influence on the gravimetric and volumetric energy density.

An alternative to this approach is the use of separators which can effectively prevent the diffusion of polysulfides. We have recently showed that ion conductive ceramics (LATP from Ohara) increased the cycling stability on over 350 cycles at 99.95% Coulombic efficiency.[22] That result points out the need to design completely new types of separators that are repulsive for polysulfides[22,23] and permeable for lithium ions. At the same time, the separator has to act as a reservoir for the electrolyte since higher amounts of electrolyte are typically required in Li-S batteries compared to Li-ion batteries.[24]

Such approach was demonstrated in our previous work[22] where a hydrophobic interlayer prepared by chemically modified rGO was used. Chemical modification has been achieved by grafting organic molecules, such as *p*-fluorophenyl groups, onto rGO. Improved capacity stabilization was attributed to the lower reactivity of long-chain polysulfides with metallic lithium, due to reduced diffusion and/or migration through the separator.

A graphene derivative rGO, with the remaining oxygen and nitrogen functional groups, offers many possibilities for tailoring the surface.[25] The covalently modified graphene materials with halogen molecules have recently drawn attention for the use in electronic applications.[26] Nair et al.[27] prepared fully fluorinated graphene sheets by using XeF_2 as a fluorinated agent. As-prepared fluorinated graphene sheets possess insulating properties and show stability in different chemical and thermal conditions. The fluorinated graphene can be considered a 2D analogue of polytetrafluoroethylene (PTFE), which is a 1D fluorinated carbon chain.

In this work, we present a new synthesis route with direct fluorination of the surface of rGO with XeF_2[28] or fluorine gas in anhydrous hydrofluoric acid (aHF). As-prepared samples were thoroughly studied by solid-state NMR spectroscopy and HAADF-STEM. The degree of fluorination was additionally determined by X-ray Photoelectron Spectroscopy (XPS). Morphological changes during the fluorination process were assessed by SEM microscopy. As-prepared samples were deposited on the glass fiber sheets used as separators in the Li-S batteries. The impact of degree of fluorination on the capacity stability is presented. XPS analysis of both electrodes (composite cathode and lithium) has been performed in order to understand the differences in reaction mechanisms occurring with and without the interlayer containing fluorinated rGO.

2. Experimental part

2.1. Preparation of the fluorinated rGO samples

Graphene oxide (GO) and reduced graphene oxide (rGO) were prepared according to known procedures.[29,30] The rGO materials were fluorinated in perfluorinated ethylene propylene (FEP) reaction vessels constructed from 16 mm i.d. (19 mm o.d.) tubing equipped with a PTFE (polytetrafluoroethylene) valve encased in a brass casing and containing a PTFE-coated magnetic stirring bar.

The solvent, aHF, was prepared by treating commercial anhydrous HF (Linde, Fluorwasserstoff 3.5) with K_2NiF_6 (Ozark-Mahoning, 99%) for several hours prior to use. Fluorine (Solvay Fluor, 98–99 vol%) and BF_3 (Union carbide, 99.5%) were used as received. Xenon difluoride was prepared photochemically by UV irradiation of a xenon-fluorine gaseous mixture according to the published procedure.[31]

Volatile fluorides, HF, F_2, and BF_3, were transferred on a vacuum line constructed of PTFE, FEP, nickel and equipped with a monel Helicoid pressure gauge, a soda lime scrubber, liquid nitrogen cooled traps, and a two-stage rotary vane pump. The solid reagent, XeF_2, was stored and handled in an argon atmosphere in a glovebox with water content less than 0.5 ppm.

Reduced graphene oxide (rGO) was weighed in air into the FEP-reaction vessel which was attached to the vacuum line via a PTFE valve and evacuated. The solvent HF was condensed at liquid nitrogen temperature into the vessel. After the mixture had been warmed to room temperature, the resulting black slurry was agitated overnight on a laboratory platform shaker to ensure the homogeneity of a suspension. To a thoroughly homogenized rGO/HF slurry fluorine gas was added on a vacuum line at liquid nitrogen temperature. The reaction mixture was agitated on a laboratory shaker at room temperature for several days. Three different samples were synthesized with the aim obtaining different ratios of fluorine reacted with rGO. The schematic presentation of the reaction is given in Figure 1. More precisely, a sample **F-rGO_2** was prepared by the fluorination of rGO (97 mg) with XeF_2 (710 mg, 4.19 mmol) and catalytic amount of Lewis acid BF_3 (0.63 mmol) in aHF (5.8 mL) for 25 days. A second sample, **F-rGO_3**, was prepared by the fluorination of rGO (109 mg) with F_2 (7.03 mmol in total, added in two portions) in aHF (5.8 mL) for 3 days. The third sample (**F-rGO_4)** was prepared by the fluorination of rGO (102 mg) with F_2 (8.19 mmol in total, added in two portions) in aHF (11.3 mL) for 51 days.

Caution: Fluorine and anhydrous hydrogen fluoride must be handled with great care in a closed system (i.e. vacuum line constructed of appropriate materials) located in a well-ventilated fume hood and protective gear must be worn at all times. Experimenters must familiarize themselves with hazards associated with the use of reactive inorganic fluorides and with the proper treatment procedures in the event of exposure.[32,33]

To prepare interlayers on the glass microfiber separator (Whatman), the fluorinated rGO samples were dispersed in the NMP and homogenously deposited. The three different separator interlayers were prepared by the deposition of an F-rGO_x dispersion (20 mg in 3 ml of NMP) on the top of glass microfiber, and dried for 4 days at 80°C, before being transferred into the glovebox and used for battery assembly. The estimated loading of F-rGO_x on top of glass microfiber separator is between 0.3 to 0.4 mg/cm^2.

2.2. Microscopy and NMR characterization

A field-emission scanning electron microscope (FE SEM Supra 35 VP Carl Zeiss) was used to obtain scanning electron microscope (SEM) images of the materials. For transmission electron microscopy (TEM) microscopy, the fluorinated F-rGO_3 sample was dispersed in ethanol and a drop of the dispersion was placed on a lacey-carbon-coated Cu grid and dried. Samples were examined with a Jeol ARM 200 CF, and a probe Cs-corrected scanning transmission electron microscope, equipped with a cold field emission electron source, operated at 80 kV. For electron energy loss spectroscopy (EELS) measurements GATAN Quantum ER dual-EELS system was used. Classical TEM-HRTEM and HAADF/ABF-STEM techniques were used for sample imaging. EELS spectra were collected in the STEM mode. To determine the ratio of intensities of individual fluorine atoms and carbon atoms from the substrate in HAADF images, models were constructed and HAADF images were calculated using the QSTEM computer program.[34]

^{13}C MAS (Magic-Angle Spinning), ^{19}F-^{13}C CPMAS (Cross-Polarization Magic-Angle Spinning) and ^{19}F-^{13}C Lee-Goldburg (LG) CPMAS NMR spectra were recorded on a 600 MHz Varian NMR system equipped with a 3.2 mm Varian probe. Larmor frequencies for ^{19}F and ^{13}C were 564.10 MHz and 150.82 MHz, respectively. Sample rotation frequency in all experiments was 12 kHz. For MAS, CPMAS and LG-CPMAS NMR measurements, the number of scans was 6400, 50000 and 20000, and repetition delays between scans were 10 s, 0.5 s and 0.25 s, respectively. ^{13}C spectra were excited by a 90° excitation pulse of 1.9 μs. ^{19}F-^{13}C CPMAS experiment employed RAMP[35] during 0.5 ms CP block and high-power XiX

heteronuclear decoupling[36] during acquisition. In the ^{19}F-^{13}C LG-CPMAS experiment, an additional tilt pulse of 0.725 μs was added prior to the 0.1 ms Lee-Goldburg[37] CP block. ^{13}C frequency axis was referenced to tetramethylsilane.

In the two-dimensional ^{19}F-^{13}C LG-HETCOR experiment, ^{19}F nuclei were first excited by a 90° pulse with a duration of 1.85 μs. Afterwards, their magnetization was allowed to evolve for t_1 before it was transferred to carbon nuclei by the 0.1 ms LG-CP block and the ^{13}C signal was detected. Prior to the LG-CP block, a tilt pulse of 0.725 μs was used. High-power XiX heteronuclear decoupling was applied on the fluorine channel during the acquisition. The number of increments along the indirectly detected dimension was 21 and the number of scans for each increment was 6000. The experiment was carried out in a hypercomplex mode.[38]

2.3. XPS characterization

XPS measurements were carried out using a Kratos Axis Ultra spectrometer with focused monochromatic Al Kα radiation (hν=1486.6 eV). The spectrometer was calibrated using Ag $3d_{5/2}$ photoemission peak with full width at half maximum (FWHM) of 0.58 eV at 368.3 eV (binding energy) and each photoemission spectrum was recorded with a constant pass energy of 20 eV. The pressure in the analysis chamber was maintained at ~5.10^{-9} mbar and the analyzed area of the samples was 300×700 μm^2. Short scan spectra were measured before and after the usual long scan experiment to check for the possible degradation of sample surfaces due to X-ray beam. The photoemission peaks were calibrated using the hydrocarbon contamination peak at 285 eV in the C 1s spectra. The core level photoemission spectra were fitted using a Shirley type background with the linear combination of 70% Gaussian and 30% lorentzian line shapes[39] and the respective peaks were quantified using Scofield's relative sensitivity factors.[40] The process of battery opening, handling of electrodes and sample analysis was done either in a controlled argon atmosphere or an ultra-high vacuum. The vacuum sealed sample packages were carefully opened inside the argon purged glovebox which is directly connected to the XPS spectrometer to avoid any air/moisture exposure in the samples.

2.4. Electrochemical characterization

Composite cathodes were prepared by mixing sulfur impregnated carbons[41] with a sulfur loading of 50 wt.%, PVdF and carbon black Printex XE2 from Degussa in a mass ratio of 80:10:10 wt.%. The mixture was dispersed in N-methylpyrolidone (NMP) and cast on

aluminum foil. The typical loading of the active material on the electrode was from 1.5 mg to 2 mg of sulfur per cm^2 electrode. The F-rGO_x interlayer was faced against a cathode, wetted with a 1 M LiTFSI in sulfolane electrolyte (60 µL per mg of sulfur) and placed into a battery sandwich together with metallic lithium (Aldrich) as a counter-electrode. The batteries were cycled in the potential range between 1.5 V and 3.0 V by using a Maccor 4200 or Biologic VMP3 galvanostat/potentiostat at C/10 (167.2 mAg^{-1}). All electrochemical measurements are given as a specific capacity calculated on the amount of sulfur in the cathode composite.

3. Results and discussion

Different degrees of fluorination of the rGO were achieved by changing the reaction parameters and time. During the synthesis, the fluorination process could be visually observed by fading black color of rGO and resulting orange (F-rGO_2), dark yellow (F-rGO_3), and eventually light yellow color (F-rGO_4) of extensively fluorinated material (Figure 1). The crucial step in the synthesis is to maintain the homogeneity of the suspension which over time becomes more thick and viscous due to the absorption of hydrogen fluoride on rGO, which necessitates the usage of relatively large amounts of HF solvent. Hydrogen fluoride also retards the subsequent reaction between rGO and fluorine. Furthermore, the aforementioned homogenization step is crucial for safety of the fluorination procedure, because dry reduced graphene oxide reacts violently with fluorine gas. Audible sparkling and local melting of fluorinated polymer occurred on inner walls of the FEP reaction vessel when dry flakes of rGO reacted with F_2 that was added at liquid nitrogen temperature shortly after the addition of solvent. It noteworthy that the fluorination process of rGO with both in this study used potent fluorination reagents (F_2 or XeF_2/BF_3) is very slow in the presence of aHF; therefore, long reaction times were required.

3.1. Characterization of F-rGO_x samples:

3.1.1. Microscopy

Morphological changes of rGO after fluorination were checked by SEM and TEM microscopy. Figure 2 presents SEM micrographs of rGO and fluorinated derivatives of rGO. Morphological differences between rGO (Figure 2a) and low degree fluorinated sample F-rGO_2 (Figure 2b) are minor, which suggests the non-destructive nature of the fluorination process. The use of fluorine gas in anhydrous HF influences the morphology of samples as the prepared F-rGO_3 (Figure 2c) and F-rGO_4 (Figure 2d) samples are more compact and dense.

Imaging the F-rGO_3 sample with conventional TEM techniques revealed overlapping sheets of fluorinated rGO (Figure 3a). On thin areas where no obvious overlapping was present, we performed HAADF-STEM imaging at atomic resolution. Spots with higher contrast were observed (Figure3b) and attributed to individual atoms or clusters of fluorine atoms. The presence of fluorine in this area was confirmed with EELS. In Figure 3c, the background subtracted EELS core-loss spectrum is shown where the edge at 685 eV that is characteristic for fluorine is clearly resolved. Due to a sub-angstrom resolution, single-atom imaging is possible, with C-corrected STEM even at 80 kV; however, the direct interpretation of the images is quite inaccurate. The diameter of the individual bright atoms in Figure 3b, defined as full-width at half maximum of line profile across the atoms, is in the order of 0.1 nm (Figures 3d and e). The covalent radius of fluorine is 71 pm, which is close to the measured value of 100 pm, but to be more exact it is necessary to compare the experimental image with a simulated (calculated) one. For this purpose, we construct the model consisting of 3 misoriented parallel sheets of graphene (turbostratic graphene) with few bonded fluorine atoms (one single and one pair with the distance of 140 pm between atoms), as shown in Figure 3f. Using suitable instrumental parameters (such as Cs and Cc values, defocus, energy spread, convergence, etc.), we calculated the HAADF image of the constructed model using the QTEM code.[34] The simulated image is presented in Figure 3g. The dimensions and the ratio of intensity of carbon substrate and individual fluorine atoms in a simulated image are in quite good agreement with experimental images. Based on these results we can conclude that atoms observed in HAADF images are indeed fluorine atoms.

The number of graphene sheets in the observed area was estimated from low-loss EELS spectra. As described by Eberlein[42], the position of the plasmon peak maximum is a function of number of sheets of graphene. The authors observed that $\pi+\sigma$ surface plasmon maxima are around 15 eV for single-sheet graphene, 17 eV for 3 sheets and approaching 24 eV in the case of 10 or more sheets. We used a similar method and found that most of thinnest areas had 3-5 graphene sheets (with $\pi+\sigma$ surface plasmon maxima at around 17 eV (Figure 3h)) in turbostratic orientation. Figure 3i with low-loss EELS spectra and a local maximum at 22 eV is an example of an area with 5–10 graphene sheets.

3.1.2. NMR

^{13}C MAS NMR spectra of our materials are presented in Figure 4. The spectra of the materials at different stages of preparation substantially differ from one another. ^{13}C MAS NMR spectrum of graphene oxide (GO) exhibits a number of partly resolved signals in the chemical

shift range between 0 and 200 ppm. As in previous NMR studies,[25,43–48] the signals resonating at 60 ppm and 70 ppm can be assigned to either C–O–C or tertiary C–OH groups, whereas the signals in the range between 110 ppm and 150 ppm belong to graphitic sp^2 carbon atoms. A weaker signal at about 166 ppm can be assigned to ester carbonyl groups O=C–O and a signal at about 190 ppm to ketones C=O. ^{13}C MAS NMR spectrum of the reduced material (rGO) is markedly different from the spectrum of the parent material. It contains one dominating broad signal extending from 90 ppm to 150 ppm and a weak signal of the O=C–O groups resonating at 166 ppm. Broad weak contributions below 60 ppm and above 200 ppm are the first-rank spinning sidebands of the main broad signal. The disappearance of the signals below 80 ppm indicates that the selected procedure for the preparation of rGO quite efficiently reduces the –C–OH and –C–O–C groups into the graphitic >C=C< carbon. The increased width of the obtained graphitic signal evidences that although the total fraction of the sp^2 carbon increases, the average dimensions of the graphitic domains decrease upon reduction.[25]

Fluorination of rGO again leads to large changes in the NMR spectrum. The ^{13}C MAS NMR spectra of the three fluorinated samples F-rGO_2, _3, and _4 (Figure 4) are very similar to one another and all exhibit at least four relatively narrow signals between 80 ppm and 170 ppm. The small line width suggests that the above described procedure of fluorination leads to well-ordered materials with well-defined fluorinated graphene sheets. In all three spectra of fluorinated samples, the highest signals are those resonating at 84 ppm, lower and broader, but also quite intense are the signals extending between 95 ppm and 120 ppm. The spectra also exhibit a pronounced narrow signal at 135 ppm. This latter signal is accompanied by two strong spinning sidebands at about 50 ppm and 220 ppm, indicating that the corresponding ^{13}C nuclei experience quite strong chemical shift anisotropy. This fact and the value of the isotropic chemical shift of 135 ppm suggest that the contribution belongs to the graphitic (or graphene-like) sp^2 carbon. This is in the agreement with observations in the TEM study, where we determined 5–10 layer thick graphene sheets. The fourth signal in the spectra of F-rGO resonates at 166 ppm and thus belongs to the remaining O=C–O groups. In all three fluorinated materials, the fraction of the O=C–O carbon atoms was small, below 3%.

To better understand the origin of the main signals in the NMR spectra of fluorinated materials, ^{19}F-^{13}C CPMAS and ^{19}F-^{13}C LG-CPMAS spectra were recorded. Examples of both spectra and their comparison to the directly excited ^{13}C MAS NMR spectrum of the F-rGO_3 are shown in Figure 5. We can see that the ^{19}F-^{13}C CPMAS spectrum exhibits the same signals as the ^{13}C MAS spectrum, except for the signal from the O=C–O groups. Obviously,

the latter groups are distant from fluorine nuclei so that the polarization transfer between ^{19}F and ^{13}C is ineffective. Gao et al. showed in their graphite oxide material that ^{13}C nuclei resonating at 169 ppm were spatially separated from the majority of the graphitic carbon.[46] If this was also the case in our materials, it would readily explain the disappearance of the 166 ppm signal in the ^{19}F-^{13}C CPMAS NMR spectrum.

The ^{19}F-^{13}C LG-CPMAS experiment is more selective than the ordinary CPMAS experiment. In this type of experiment, the polarization transfer between ^{19}F and ^{13}C nuclei is efficient only for very proximal (e.g. directly bound) nuclei. Polarization transfer to carbon nuclei that are more than one bond apart from fluorine is already substantially hampered and leads to a notable reduction of the ^{13}C NMR signal. The ^{19}F-^{13}C LG-CPMAS NMR spectrum of F-rGO_3 clearly shows that only the narrow signal at 84 ppm and the broad signal between 95 ppm and 120 ppm belong to the fluorinated carbon atoms. The graphitic sp^2 carbon atoms resonating at 135 ppm, on the other hand, are not directly bound to fluorine. Based on the values of the isotropic chemical shifts, the 84 ppm ^{13}C signal could be assigned to the fluorinated carbon atoms within the core of the modified graphene sheets (–C–F), and the signal between 95 ppm and 120 ppm could be ascribed to the fluorinated carbon atoms on the edges of such sheets. This assumption was further verified by the two-dimensional ^{19}F-^{13}C heteronuclear correlation (LG-HETCOR) experiment. The LG-HETCOR NMR spectrum of F-rGO_3 in Figure 5 shows four distinct ^{19}F-^{13}C cross peaks. The most intense one resonates at 84 ppm and -145 ppm along the ^{13}C and ^{19}F dimensions, respectively, and, as already mentioned, belongs to the –C–F motifs within the fluorinated sheets. The graphitic carbon nuclei resonating at 135 ppm also yield a weak cross peak with the fluorine nuclei resonating at about -145 ppm. This indicates that the non-fluorinated sp^2 carbon and the –C–F carbon share the same fluorinated graphene sheets and that the two types of carbon are quite homogeneously dispersed throughout the sheets. Careful inspection of the slices through the LG-HETCOR spectrum along the ^{19}F dimension shows that the most intense cross peak is actually accompanied by a pronounced low-frequency shoulder. This shoulder with ^{19}F chemical shift of about -170 ppm could be due to –C–F pairs, whose nearest neighbors in the fluorinated graphene sheets are again –C–F pairs. The large intensity of the shoulder suggests that such fluorine-rich parts of the sheets are quite big or quite abundant, and that the extent of fluorination in the F-rGO samples is large.

The remaining two distinct cross peaks in the LG-HETCOR spectrum resonate at about 105 ppm and -130 ppm, and at 111 ppm and -50 ppm along the ^{13}C and ^{19}F dimensions,

respectively. The ^{19}F chemical shift of the former cross peak is very close to the ^{19}F chemical shift of the most intense signal in the LG-HETCOR spectrum, suggesting that it most probably also corresponds to the –C–F type of fluorine. The different ^{13}C chemical shifts between the two –C–F contributions could stem from the difference in the aromatic character of the corresponding carbon rings; whereas the 84 ppm signal can be assigned to –C–F groups in the parts of the fluorinated sheets with the predominantly non-aromatic character, the 105 ppm signal could be ascribed to the –C–F groups in the parts of the sheets with a more aromatic character. The cross peak resonating at 111 ppm and -50 ppm along the ^{13}C and ^{19}F dimensions, respectively, exhibits a very different fluorine chemical shift and this is most probably the contribution of the fluorinated $–CF_2$ groups at the edges of the fluorinated graphene sheets. A tentative model of F-rGO materials is sketched in an inset in Figure 5.

The ^{19}F chemical shift of about -50 ppm could also perhaps be assigned to fluorine bonded to nitrogen. Reduction of GO by hydrazine can, namely, create some hydrazine, amine or aziridine groups on the surface of rGO.[25] During the subsequent fluorination, hydrogen atoms in such groups could be substituted by fluorine, and the obtained –C–N–F motifs could perhaps contribute to NMR signals with a ^{13}C chemical shift above 100 ppm and ^{19}F chemical shift above -60 ppm. However, a relatively large distance between C and F in such functional groups would make their contribution hardly detectable in the LG-CPMAS and LG-HETCOR experiments, meaning that the –C–N–F motifs are not consistent with our NMR spectra.

A quantitative analysis of ^{13}C MAS NMR spectra of the F-rGO materials allows one to estimate the degree of fluorination of these materials. In fact, a brief look at the spectra and comparison of the heights of the –C–F and the sp^2 signals already suggests that the degree of fluorination is the lowest for F-rGO_2, and that F-rGO_3 and F-rGO_4 are fluorinated to approximately the same extent (Figure 4). The detailed decomposition of the ^{13}C MAS NMR spectra into individual contributions enables an even more precise estimation (Figure 5). Summing up the contributions of the –C–F and $–CF_2$ groups, we can see that in F-rGO_2 there are 67%, in F-rGO_3 there are 74% and in F-rGO_4 there are 76% of fluorinated carbon atoms. Obviously, the extent of fluorination is rather high in all three samples.

3.2. Use of F-rGO samples in Li-S batteries:

3.2.1. Electrochemical characterization

To evaluate the impact of fluorination, we prepared four different sets of batteries. All tested batteries were prepared by using cathodes from the same batch while the amount of

electrolyte was normalized to the amount of sulfur in the cathode. The difference between cells was in the interlayer between the cathode and lithium metal. A typical cross-section and top view of a separator interlayer is presented in Figure 6. Based on many cross-section thickness measurements, we can estimate that the average thickness is approximately 3 μm (Figure 6a). We need to emphasize that the preparation procedure for the deposition of fluorinated reduced graphene oxide was not optimized and some imperfections can be observed from the top-down view in Figure 6b.

During assembly of the Li-S cells, the interlayer was faced to the surface of the cathode. A typical open circuit potential (OCP) of the Li-S cells with fluorinated interlayer was between 3.3 and 3.4 V versus metallic lithium. The OCP voltage is about 200–300 mV higher than the OCP in our previous paper where chemically modified graphene oxide was used as an interlayer.[22] The observed voltage could be an indirect confirmation for the presence of the elemental fluorine since the OCV voltage fits very well with the OCV voltage of Li $(C–F)_n$ batteries.[49,50] The presence of free fluorine is additionally confirmed by the presence of a plateau at 3.1 V during the first discharge. The length of the plateau is correlated with a degree of fluorination (Figure S1); however, according to the quantity of fluorine in the interlayer, only a minor part of fluorine electrochemically reacts with lithium. We assume that the observed electrochemical reaction in the first discharge is correlated to the amount of "free" fluorine in the interlayer. The reduction of fluorine is accomplished during the first discharge and batteries are cycled as normal Li-S cells from the second cycle.

The degree of fluorination was additionally measured by XPS, which confirmed the trend observed by NMR, namely F-rGO_2 contains 17 mol% of fluorine while F-rGO_3 and F-rGO_4 contain 43 mol% of fluorine (hydrogen is not taken into account because not detected by XPS). The C1s spectrum of F-rGO_3 sample is shown in Figure S2. According to XPS, F-rGO_3 mainly contains C–F groups (~95%) and a few CF_2 groups (~5%), which is in good agreement with NMR data.

With the aim of determining how different degrees of fluorination and different reaction times influence the electrochemical stability of Li-S batteries, we prepared 4 different sets of batteries using the same cathode material and electrolyte (quantity of electrolyte was normalized per sulfur mass in the electrode). Figure 7 shows the capacities obtained during discharge process for four different separators. The highest discharge capacities were obtained within batteries without an rGO interlayer and with samples with the lowest degree of fluorination (sample F-rGO_2). Despite high starting capacities in both measurements, we observed relatively fast fading in the first 3 cycles; however, remarkable differences between

capacities have to be pointed out. The capacity drop in the battery containing separator with the interlayer of F-rGO_2 is only half of the capacity drop in the battery without interlayer. Much better cycling stability in the formation cycles was obtained with more fluorinated graphene interlayers; however, starting discharge capacities were lower compared to batteries with an F-rGO_2 interlayer or without any interlayer. This is correlated to the transport properties for lithium ions. A higher degree of fluorination is expected to result in a more hydrophobic nature of the interlayer as well as denser and more compact sample morphologies. Thus, it is not surprising that the battery with the interlayer prepared from sample F-rGO_4 showed the lowest capacity at the beginning. The optimal cycling behavior (cycling stability and specific capacity) was obtained with the interlayer prepared from the F-rGO_3 sample. That set of measurements confirms the blocking nature of fluorinated rGO samples and points out the need for proper design of the blocking interlayer on the separator. A higher degree of fluorination leads to low specific capacities due to transport properties, while a lower degree of fluorination slightly improves capacity fading. By adjusting the degree of fluorination (that can be correlated to the hydrophobicity) and by optimization of the interlayer morphology and deposition, we assume that stable cycling properties can be obtained. So far, the electrochemical properties of Li-S batteries containing F-rGO_3 are optimal and are very similar to the cycling properties with an interlayer prepared by the chemical modification of rGO shown recently.[22] The observed capacity fading can be correlated to the imperfections in the deposited interlayers (Figure 6a).

Comparison of the galvanostatic curves reveals further differences in the electrochemical properties of tested separator interlayers. Figure 8 shows selected voltage profiles for all battery configurations tested in this study for the 2nd, the 10th, the 50th and the 100th cycles. It should be noted that the first cycle was not reported in the voltage profiles since it corresponds to the reaction of lithium with free fluorine, as stated above. As a result, the second cycle can be considered the reference cycle.

The battery with the glass fiber separator exhibits galvanostatic curves with a relatively short high voltage plateau and ill-defined low voltage plateau, suggesting high internal resistance inside the cell, which is probably connected to a high capacity drop in the first cycle (Figure 8a). Much smaller increase of polarization, but still remarkable, were observed in the battery using F-rGO_2 sample as the interlayer (Figure 8b). Comparison between those two samples confirms blocking nature for the polysulfides of the fluorinated interlayer. The use of interlayers with a higher degree of fluorination (Figure 8c,d) improves capacity stability and capacity drop is mainly connected with a capacity fading related to a low voltage plateau

(characteristic to formation of the short polysulfides and Li_2S). Here, we need to pinpoint that voltage plateau is more sloping in the batteries with a higher degree of fluorination (with F-rGO_3and F-rGO_4 interlayers) compared to the battery with an F-rGO_2 interlayer. The difference can be explained by a decrease of ionic pathways for lithium ions due to the higher hydrophobicity and denser layers. The latter property is also the reason for different specific capacities between F-rGO_3and F-rGO_4 interlayers, while the cycling stability is not affected. That was expected, since both samples have the same degree of fluorination; however, much longer reaction times for F-rGO_4 sample correspond to denser samples.

3.2.2. Study of mechanisms by XPS

In order to understand the mechanisms and the origin of the electrochemical improvements of the Li-S batteries using F-rGO samples, we carried out the XPS study of electrodes from batteries with and without F-rGO in the separator. Both electrodes (composite cathode and lithium) were analyzed at the end of discharge and charge of the first and second cycle.

The main interest of XPS analysis in our approach is that it allows a clear distinction between the different chemical environments of sulfur, and therefore between the different sulfur-containing species in the system, due to the wide binding energy range of S 2p core peak as a function of oxidation state and local environment of sulfur atoms. As shown in our previous work, the salt LiTFSI, polysulfides S_n^{2-}, lithium sulfide Li_2S and possible extra species coming from side reactions can be distinguished in S 2p spectra.[13] Moreover, it is possible to distinguish terminal and bridging sulfur atoms in polysulfides, and thus obtain information about the mean length of polysulfides from the terminal vs. bridging sulfur intensity ratio.

The XPS study was carried out on the F-rGO_3 sample which gave the best electrochemical performances in Li-S batteries, as shown above. The first and the second cycles were studied. In order to have full information on sulfur species present in the electrolyte, which are the electrochemically active species, the electrodes were not washed before XPS analysis but just dried in an ultra-high vacuum after battery opening without removing the salt.

First cycle

The S 2p XPS spectra of the composite cathode, just after simple contact with the electrolyte, and after the first discharge, with the reference glass fiber separator and with the F-rGO_3 interlayer, respectively, are plotted in Figure 9. The cathode that was only in contact with the electrolyte (soaked electrode) shows the S 2p signal of the salt LiTFSI at very high binding energy (S $2p_{3/2}$ at around 169.4 eV[51]) together with the signal of the starting elemental sulfur

S_8 (S $2p_{3/2}$ at ~164 eV). Note that due to spin-orbit coupling, all S 2p components consist of doublets ($2p_{3/2}$ - $2p_{1/2}$) separated by ~1.2 eV with a 2/1 intensity ratio. Only the position of the S $2p_{3/2}$ component will be further analyzed. After the first discharge, the S 2p spectrum of the cathode from the battery using the reference glass fiber separator is very different from the soaked electrode. New components appear which are assigned to Li_2S (~160.5 eV), to terminal sulfur (~162 eV) and bridging (~163.6 eV) sulfur atoms from Li_2S_n polysulfides, respectively. The contribution of bridging sulfur is very weak, showing that the mean length of polysulfides is very short in this case (mainly Li_2S_2). This is the result of a reduction of S_8 upon discharge, leading to the final reduction product Li_2S and to very short chain polysulfides. Note that an additional peak appears at ~167 eV. This binding energy value is in the range of S(IV) oxidation state, and can be assigned to sulfite compounds arising from the reduction of the salt $(F_3C\text{-}SO_2)_2N^-,Li^+$ (LiTFSI) in which sulfur is originally in the S(VI) oxidation state. Several side reaction products can be considered to explain this peak, such as $LiSO_2CF_3$ after breaking the S–N bond of LiTFSI, or $(F_3C\text{-}SO_2\text{-}N\text{-}\underline{S}O_2)^{2-},2Li^+$ after breaking the S–C bond, or even Li_2SO_3, as already mentioned by Aurbach *et al.*[52]

On the other hand, the S 2p spectrum of the cathode coming from the battery using the F-rGO interlayer shows a main contribution of bridging sulfur atoms (~163.6 eV) with a bridging to terminal sulfur intensity ratio ~4, and no signal for Li_2S. Therefore, at the end of the first discharge, a rather weak proportion of S_8 has been reduced. Note that the electrodes were not washed before XPS analysis, as said above, and thus the S 2p signal of the salt may fluctuate as a function of the amount of electrolyte remaining at the surface of the electrode, depending on the wettability of it, which may change after cycling.

At the same time, analysis of F 1s spectra of the separator provides interesting information, as shown in Figure 10. After the first discharge, the F 1s spectrum of the reference glass fiber separator shows two peaks (Figure 10a). The first at 688.6 eV corresponds to the LiTFSI salt.[51] The weak one at 685 eV is attributed to LiF, coming from the degradation of salt. The F 1s spectrum of the separator containing the F-rGO interlayer has a very different shape (Figure 10b) since the LiF signal shows a much greater intensity (5% of the global XPS intensity, vs. 0.8% for the reference glass fiber separator). For comparison, the F 1s spectrum of the pristine F-rGO_3 sample is plotted in Figure 10c. We can conclude that the peak observed at 685 eV after discharge cannot be attributed to fluorinated species from F-rGO, but results from reaction of lithium towards F-rGO. This allows understanding of the mechanisms occurring upon the first discharge: «activation» process of the F-rGO interlayer occurs which consists of the reaction of lithium with the free fluorine remaining in the separator to produce

LiF. As a result, a rather weak proportion of S_8 is reduced. Therefore, the battery can be considered operational only after this «activation» cycle, and the second cycle can be considered the true reference cycle for cycling evolution upon aging. That is why we propose a detailed analysis of the second cycle.

Second cycle

The same batteries were studied, one with the reference glass fiber separator and the other one with the F-rGO_3 interlayer. Both the composite cathode and the lithium anode were analyzed, at the end of the second discharge, and at the end of the second cycle (second charge). The results obtained for the cathode are shown in Figure 11a (2^{nd}discharge) and 11b (2^{nd} charge).

The S 2p spectra of both cathodes after the 2^{nd} discharge show the expected profile, *i.e.* the main contribution of the Li_2S signal, which is the final reduction product, together with the presence of very short chain polysulfides (bridging to terminal sulfur intensity ratio close to 0.16 corresponding to a mean Li_2S_n length n~2.3). The signals of the salt LiTFSI and its reduction product(s) are also detected. On the other hand, the S 2p spectra of both cathodes after the 2^{nd} charge (Figure 11b) exhibit some interesting differences. Both cathodes display the two signals of bridging (~163.5 eV) and terminal (~162 eV) sulfur atoms from polysulfides, but with different intensity ratios. Note that, as said above, the amount of remaining salt at the surface may fluctuate and, for that reason, the signal of the polysulfides for the cathode using the F-rGO interlayer was zoomed. For the cathode using the reference glass fiber separator, the contribution of terminal sulfur atoms is much greater, which corresponds to an estimated mean polysulfide length $Li_2S_{4.2}$, whereas for the cathode using the F-rGO_3 interlayer separator the contribution of terminal sulfur atoms is rather weak. The great bridging to terminal sulfur intensity ratio ~4.6, together with the slightly greater binding energy observed for the bridging sulfur peak (164 eV), shows that elemental sulfur is present at the end of charge for this sample. Therefore, the reversibility of the electrochemical reaction appears to be much better for the cathode using the F-rGO_3 interlayer separator: more short-chain polysulfides have been re-oxidized into long-chain polysulfides and elemental sulfur upon charge.

Analysis of the lithium electrode provides additional information about the mechanisms. S 2p spectra of the two lithium electrodes using the two kinds of separators are shown in Figure 12a (2^{nd} discharge) and 12b (2^{nd} charge). These spectra display the same S 2p components as cathodes.

The spectrum of the lithium electrode using the reference glass fiber separator after the 2nd discharge shows the presence of Li_2S (~160.2 eV) and of very short-chain polysulfides (estimated mean length $Li_2S_{2.2}$). These species are the result of longer-chain polysulfides reduction at the surface of metallic lithium, ensuing from the diffusion/migration of polysulfides from the cathode to the lithium electrode, and represent a loss of reversible capacity for the following charge at the cathode side. When it comes to the Li electrode using the F-rGO interlayer separator, no Li_2S signal can be detected, and the amount of polysulfides is weaker. This is the proof that the F-rGO interlayer has been very efficient in blocking the diffusion/migration of polysulfides, although some of them have reached the lithium electrode to be reduced at its surface.

After the 2nd charge (full 2nd cycle) the Li_2S signal is still present at the surface of the lithium electrode using the normal glass separator. The slight variation of the amount of Li_2S/polysulfides at the surface of this electrode compared to the discharge may be due to the surface reconstruction of metallic lithium upon charge. Concerning the lithium electrode using the F-rGO interlayer, still no Li_2S signal could be detected. Therefore, this confirms that the F-rGO plays a role in blocking the diffusion/migration of polysulfides from one electrode to the other and preventing the redox shuttle effect.

4. Conclusions

In this work, we have synthesized F-rGO by direct fluorination of reduced graphene oxide and obtained different degrees of fluorination. Characterization by NMR and TEM confirmed the formation of C–F bonds in as-prepared samples. We have used F-rGO as a separator interlayer in Li-S batteries and showed that it improves the electrochemical performances of the batteries, with a more beneficial effect for fluorine-rich F-rGO samples. XPS investigation of the action mechanisms of this interlayer additive, by comparison of the relative amounts of Li_2S, and polysulfides, by determination of the mean length of polysulfides at both electrodes, has proven the efficiency of this kind of separator interlayer in blocking the diffusion/migration of polysulfides from the porous positive electrode to the metallic lithium electrode. Above mentioned shows a better reversibility of the sulfur electrochemical reaction, and better capacity retention upon cycling. The results of this work open the way to designing better selective separator interlayers in order to reach better capacity retention and finally meet requirements for the commercialization of Li-S batteries.

Acknowledgements

AV acknowledges study at University of Ljubljana, Faculty of Chemistry and Chemical Technology. This research has received funding from the Slovenian Research Agency (J2-5469) and the European Union Seventh Framework Programme under grant agreement No. 314515 (EUROLIS).

References

(1) Bruce, P. G.; Freunberger, S. A.; Hardwick, L. J.; Tarascon, J.-M. Li-O_2 and Li-S Batteries with High Energy Storage. *Nat. Mater.* **2012**, *11*, 19–29.

(2) Zhao-Karger, Z.; Zhao, X.; Wang, D.; Diemant, T.; Behm, R. J.; Fichtner, M. Performance Improvement of Magnesium Sulfur Batteries with Modified Non-Nucleophilic Electrolytes. *Adv. Energy Mater.* **2015**, *5*, DOI: 10.1002/aenm.201401155.

(3) Wenzel, S.; Metelmann, H.; Raiß, C.; Dürr, A. K.; Janek, J.; Adelhelm, P. Thermodynamics and Cell Chemistry of Room Temperature Sodium/Sulfur Cells with Liquid and Liquid/Solid Electrolyte. *J. Power Sources* **2013**, *243*, 758–765.

(4) Armand, M.; Tarascon, J.-M. Building Better Batteries. *Nature* **2008**, *451*, 652–657.

(5) Dunn, B.; Kamath, H.; Tarascon, J.-M. Electrical Energy Storage for the Grid: A Battery of Choices. *Science* **2011**, *334*, 928–935.

(6) Rauh, R. D.; Shuker, F. S.; Marston, J. M.; Brummer, S. B. Formation of Lithium Polysulfides in Aprotic Media. *J. Inorg. Nucl. Chem.* **1977**, *39*, 1761–1766.

(7) Mikhaylik, Y. V.; Akridge, J. R. Polysulfide Shuttle Study in the Li/S Battery System. *J. Electrochem. Soc.* **2004**, *151*, A1969–A1976.

(8) Ji, X.; Lee, K. T.; Nazar, L. F. A Highly Ordered Nanostructured Carbon-Sulphur Cathode for Lithium-Sulphur Batteries. *Nat. Mater.* **2009**, *8*, 500–506.

(9) Manthiram, A.; Fu, Y.; Chung, S.-H.; Zu, C.; Su, Y.-S. Rechargeable Lithium–Sulfur Batteries. *Chem. Rev.* **2014**, *114*, 11751–11787.

(10) Yin, Y. X.; Xin, S.; Guo, Y. G.; Wan, L. J. Lithium-Sulfur Batteries: Electrochemistry, Materials, and Prospects. *Angew. Chem. Int. Ed.* **2013**, *52*, 13186–13200.

(11) Evers, S.; Nazar, L. F. New Approaches for High Energy Density Lithium-Sulfur Battery Cathodes. *Acc. Chem. Res.* **2013**, *46*, 1135–1143.

(12) He, G.; Evers, S.; Liang, X.; Cuisinier, M.; Garsuch, A.; Nazar, L. F. Tailoring Porosity in Carbon Nanospheres for Lithium-Sulfur Battery Cathodes. *ACS Nano* **2013**, *7*, 10920–10930.

(13) Lapornik, V.; Novak Tusar, N.; Ristic, A.; Chellappan, R. K.; Foix, D.; Dedryvère, R.; Gaberscek, M.; Dominko, R. Manganese Modified Zeolite Silicalite-1 as Polysulphide Sorbent in Lithium Sulphur Batteries. *J. Power Sources* **2015**, *274*, 1239–1248.

(14) Evers, S.; Yim, T.; Nazar, L. F. Understanding the Nature of Absorption/Adsorption in Nanoporous Polysulfide Sorbents for the Li–S Battery. *J. Phys. Chem. C* **2012**, *116*, 19653–19658.

(15) Dominko, R.; Demir-Cakan, R.; Morcrette, M.; Tarascon, J.-M. Analytical Detection of Soluble Polysulphides in a Modified Swagelok Cell. *Electrochem. Commun.* **2011**, *13*, 117–120.

(16) Patel, M. U. M.; Demir-Cakan, R.; Morcrette, M.; Tarascon, J.-M.; Gaberscek, M.; Dominko, R. Li-S Battery Analyzed by UV/vis in Operando Mode. *ChemSusChem* **2013**, *6*, 1177–1181.

(17) Patel, M. U. M.; Arčon, I.; Aquilanti, G.; Stievano, L.; Mali, G.; Dominko, R. X-Ray Absorption near-Edge Structure and Nuclear Magnetic Resonance Study of the Lithium-Sulfur Battery and its Components. *ChemPhysChem* **2014**, *15*, 894–904.

(18) Wang, B.; Li, K.; Su, D.; Ahn, H.; Wang, G. Superior Electrochemical Performance of Sulfur/Graphene Nanocomposite Material for High-Capacity Lithium-Sulfur Batteries. *Chem. Asian J.* **2012**, *7*, 1637–1643.

(19) Wang, X.; Wang, Z.; Chen, L. Reduced Graphene Oxide Film as a Shuttle-Inhibiting Interlayer in a Lithium–Sulfur Battery. *J. Power Sources* **2013**, *242*, 65–69.

(20) Su, Y.-S.; Manthiram, A. A New Approach to Improve Cycle Performance of Rechargeable Lithium-Sulfur Batteries by Inserting a Free-Standing MWCNT Interlayer. *Chem. Commun.* **2012**, *48*, 8817–8819.

(21) Su, Y.-S.; Manthiram, A. Lithium–Sulphur Batteries with a Microporous Carbon Paper as a Bifunctional Interlayer. *Nat. Commun.* **2012**, *3*, 1166.

(22) Vizintin, A.; Patel, M. U. M.; Genorio, B.; Dominko, R. Effective Separation of Lithium Anode and Sulfur Cathode in Lithium-Sulfur Batteries. *ChemElectroChem* **2014**, *1*, 1040–1045.

(23) Bauer, I.; Thieme, S.; Brückner, J.; Althues, H.; Kaskel, S. Reduced Polysulfide Shuttle in Lithium–Sulfur Batteries Using Nafion-Based Separators. *J. Power Sources* **2014**, *251*, 417–422.

(24) Brückner, J.; Thieme, S.; Grossmann, H. T.; Dörfler, S.; Althues, H.; Kaskel, S. Lithium–Sulfur Batteries: Influence of C-Rate, Amount of Electrolyte and Sulfur Loading on Cycle Performance. *J. Power Sources* **2014**, *268*, 82–87.

(25) Dreyer, D. R.; Park, S.; Bielawski, C. W.; Ruoff, R. S. The Chemistry of Graphene Oxide. *Chem. Soc. Rev.* **2010**, *39*, 228–240.

(26) Karlický, F.; Kumara Ramanatha Datta, K.; Otyepka, M.; Zbořil, R. Halogenated Graphenes: Rapidly Growing Family of Graphene Derivatives. *ACS Nano* **2013**, *7*, 6434–6464.

(27) Nair, R. R.; Ren, W.; Jalil, R.; Riaz, I.; Kravets, V. G.; Britnell, L.; Blake, P.; Schedin, F.; Mayorov, A. S.; Yuan, S.; *et al.* Fluorographene: A Two-Dimensional Counterpart of Teflon. *Small* **2010**, *6*, 2877–2884.

(28) Tramšek, M.; Žemva, B. Synthesis, Properties and Chemistry of Xenon(II) Fluoride. *Acta Chim. Slov.* **2006**, *53*, 105–116.

(29) Marcano, D. C.; Kosynkin, D. V; Berlin, J. M.; Sinitskii, A.; Sun, Z.; Slesarev, A.; Alemany, L. B.; Lu, W.; Tour, J. M. Improved Synthesis of Graphene Oxide. *ACS Nano* **2010**, *4*, 4806–4814.

(30) Stankovich, S.; Dikin, D. A.; Piner, R. D.; Kohlhaas, K. A.; Kleinhammes, A.; Jia, Y.; Wu, Y.; Nguyen, S. T.; Ruoff, R. S. Synthesis of Graphene-Based Nanosheets via Chemical Reduction of Exfoliated Graphite Oxide. *Carbon* **2007**, *45*, 1558–1565.

(31) Šmalc, A.; Lutar, K.; Kinkead, S. A. Xenon Difluoride (Modification). In *Inorganic Syntheses;* Grimes, R. N., Eds.; John Wiley & Sons, Inc.: Hoboken, NJ, USA, 1992; Vol. 29, pp 1–4.

(32) Peters, D.; Miethchen, R. Symptoms and Treatment of Hydrogen Fluoride Injuries. *J. Fluorine Chem.* **1996**, *79*, 161–165.

(33) Segal, E. B. First Aid for a Unique Acid, HF: A Sequel. *Chem. Health Saf.* **2000**, *7*, 18–23.

(34) Koch, C. Determination of Core Structure Periodicity and Point Defect Density along Dislocations, Ph.D. Thesis, Arizona State University, 2002.

(35) Metz, G.; Wu, X. L.; Smith, S. O. Ramped-Amplitude Cross Polarization in Magic-Angle-Spinning NMR. *J. Magn. Reson., Ser. A* **1994**, *110*, 219–227.

(36) Detken, A.; Hardy, E. H.; Ernst, M.; Meier, B. H. Simple and Efficient Decoupling in Magic-Angle Spinning Solid-State NMR: The XiX Scheme. *Chem. Phys. Lett.* **2002**, *356*, 298–304.

(37) Ladizhansky, V.; Vega, S. A Method for Measuring Heteronuclear (^{1}H–^{13}C) Distances in High Speed MAS NMR. *J. Am. Chem. Soc.* **2000**, *122*, 3465–3472.

(38) States, D. J.; Haberkorn, R. A.; Ruben, D. J. A Two-Dimensional Nuclear Overhauser Experiment with Pure Absorption Phase in Four Quadrants. *J. Magn. Reson.* **1982**, *48*, 286–292.

(39) Shirley, D. High-Resolution X-Ray Photoemission Spectrum of the Valence Bands of Gold. *Phys. Rev. B* **1972**, *5*, 4709–4714.

(40) Scofield, J. H. Hartree-Slater Subshell Photoionization Cross-Sections at 1254 and 1487 eV. *J. Electron. Spectrosc. Relat. Phenom.* **1976**, *8*, 129–137.

(41) Fechler, N.; Fellinger, T. P.; Antonietti, M. "Salt Templating": A Simple and Sustainable Pathway toward Highly Porous Functional Carbons from Ionic Liquids. *Adv. Mater.* **2013**, *25*, 75–79.

(42) Eberlein, T.; Bangert, U.; Nair, R.; Jones, R.; Gass, M.; Bleloch, A.; Novoselov, K.; Geim, A.; Briddon, P. Plasmon Spectroscopy of Free-Standing Graphene Films. *Phys. Rev. B* **2008**, *77*, 233406.

(43) He, H.; Riedl, T.; Lerf, A.; Klinowski, J. Solid-State NMR Studies of the Structure of Graphite Oxide. *J. Phys. Chem.* **1996**, *100*, 19954–19958.

(44) Lerf, A.; He, H.; Forster, M.; Klinowski, J. Structure of Graphite Oxide Revisited. *J. Phys. Chem. B* **1998**, *102*, 4477–4482.

(45) Cai, W.; Piner, R. D.; Stadermann, F. J.; Park, S.; Shaibat, M. A; Ishii, Y.; Yang, D.; Velamakanni, A.; An, S. J.; Stoller, M.; *et al.* Synthesis and Solid-State NMR Structural Characterization of ^{13}C-Labeled Graphite Oxide. *Science* **2008**, *321*, 1815–1817.

(46) Gao, W.; Alemany, L. B.; Ci, L.; Ajayan, P. M. New Insights into the Structure and Reduction of Graphite Oxide. *Nat. Chem.* **2009**, *1*, 403–408.

(47) Casabianca, L. B.; Shaibat, M. A.; Cai, W. W.; Park, S.; Piner, R.; Ruoff, R. S.; Ishii, Y. NMR-Based Structural Modeling of Graphite Oxide Using Multidimensional ^{13}C Solid-State NMR and Ab Initio Chemical Shift Calculations. *J. Am. Chem. Soc.* **2010**, *132*, 5672–5676.

(48) Park, S.; Hu, Y.; Hwang, J. O.; Lee, E.-S.; Casabianca, L. B.; Cai, W.; Potts, J. R.; Ha, H.-W.; Chen, S.; Oh, J.; *et al.* Chemical Structures of Hydrazine-Treated Graphene Oxide and Generation of Aromatic Nitrogen Doping. *Nat. Commun.* **2012**, *3*, 638.

(49) Morita, A.; Iijima, T.; Fujii, T.; Ogawa, H. Evaluation of Cathode Materials for the Lithium/ Carbonmonofluoride Battery. *J. Power Sources* **1980**, *5*, 111–125.

(50) Watanabe, N.; Endo, M.; Ueno, K. Cathodic Discharge of Graphite Fluoride, $(CF)_n$, Prepared from Several Carbon Materials, in Lithium Organic Electrolyte Batteries. *Solid State Ionics* **1980**, *1*, 501–507.

(51) Dedryvère, R.; Leroy, S.; Martinez, H.; Blanchard, F.; Lemordant, D.; Gonbeau, D. XPS Valence Characterization of Lithium Salts as a Tool to Study Electrode/Electrolyte Interfaces of Li-Ion Batteries. *J. Phys. Chem. B* **2006**, *110*, 12986–12992.

(52) Aurbach, D.; Pollak, E.; Elazari, R.; Salitra, G.; Kelley, C. S.; Affinito, J. On the Surface Chemical Aspects of Very High Energy Density, Rechargeable Li–Sulfur Batteries. *J. Electrochem. Soc.* **2009**, *156*, A694–A702.

Figure 1: Synthesis scheme of fluorinated reduced graphene oxide samples preparation (a) and photographs of reduced graphene oxide and fluorinated samples (b).

Figure 2: SEM micrographs of rGO (a), F-rGO_2 (b), F-rGO_3 (c) and F-rGO_4 (d).

Figure 3: TEM micrograph of fluorinated graphene sheets (a). HAADF image of a thin area in the sample where individual atoms and clusters of fluorine atoms are visible (b), EELS spectrum of the area shown in Fig. 3b with characteristic fluorine K edge at 685 eV. Enlarged image of the fluorine atom (d) with the diameter (full width at half maximum) of around 0.1 nm as measured from the line profile of the intensities (e). Model of 3 layered graphene with one isolated atom and one two-atom clusters of fluorine (f) used for HAADF image calculations, shown in (g). Thickness (number of graphene layers) was estimated from the local maximum at the low loss between 12 and 30 eV as in the case of 3 – 5 layers with maximum around 17 eV (h) and 5 – 10 layers with a maximum around 22 eV (i) .

Figure 4: ^{13}C MAS NMR spectra of materials at different stages of preparation. Asterisks denote spinning sidebands.

Figure 5: A more detailed NMR analysis of F-rGO_3. (a) compares ^{13}C MAS, ^{19}F-^{13}C CPMAS and ^{19}F-^{13}C LG-CPMAS NMR spectra. Vertical lines are guides for eyes and mark positions of the O=C-O, graphitic, CF_2 and C-F carbon signals (with aromatic C^a and non-aromatic C^{na} character). Below the ^{13}C MAS NMR spectrum, decomposition of this spectrum into individual contributions is presented. The thin red line represents the model spectrum. (b) shows ^{19}F-^{13}C LG-HETCOR NMR spectrum; inset shows a tentative model of the fluorinated graphene.

Figure 6: SEM micrograph of separator cross section showing thickness of the F-rGO_X thickness (a) and bird's eye view of the homogeneity of deposited F-rGO_X interlayer on the fiber glass separator (b).

Figure 7: Cycling performance of 4 different sets of Li–S batteries (left y axis) and corresponding coloumbic efficiency (right y axis).

Figure 8: Galvanostatic discharge/charge curves for the 2^{nd}, 10^{th}, 50^{th} and 100^{th} cycle for a battery with a glass fiber separator (a), a separator with an F-rGO_2 interlayer (b), a separator with an F-rGO_3 interlayer (c) and a separator with an F-rGO_4 interlayer (d).

Figure 9: S 2p spectra of the composite cathode after simple contact with the electrolyte (soaked), after the first discharge with the reference glass fiber separator and with the F-rGO_3 interlayer.

Figure 10: F 1s spectra of the separator recovered from the battery after the first discharge: reference glass fiber separator (a) and separator including the F-rGO_3 interlayer (b). Comparison with pristine F-rGO_3, as prepared by direct fluorination of rGO (c).

Figure 11: S 2p spectra of the composite cathode with the reference glass fiber separator and with the F-rGO_3 interlayer after the 2^{nd} discharge (a) and after the 2^{nd} charge (b).

Figure 12: S 2p spectra of the lithium electrode with the reference glass fiber separator and with the F-rGO_3 interlayer after the 2^{nd} discharge (a) and after the 2^{nd} charge (b).

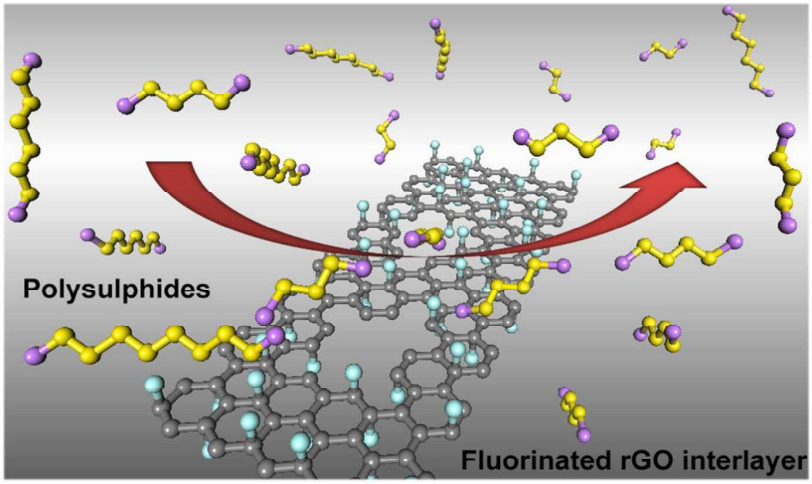

Schematic view of Lithium polysulfide repulsion from the fluorinated rGO interlayer in a Li-S battery

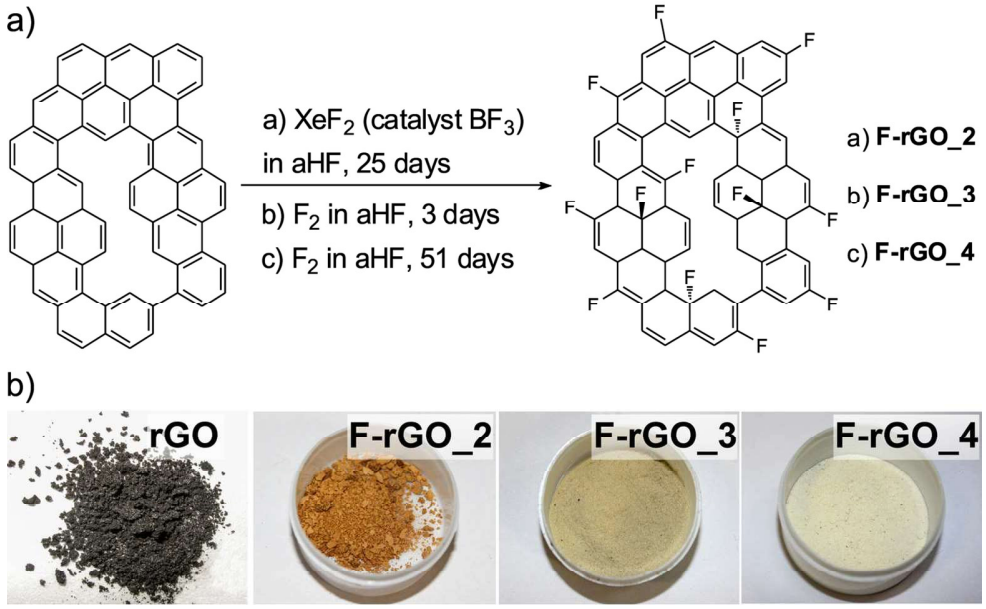

Figure 1: Synthesis scheme of fluorinated reduced graphene oxide samples preparation (a) and photographs of reduced graphene oxide and fluorinated samples (b).
129x80mm (300 x 300 DPI)

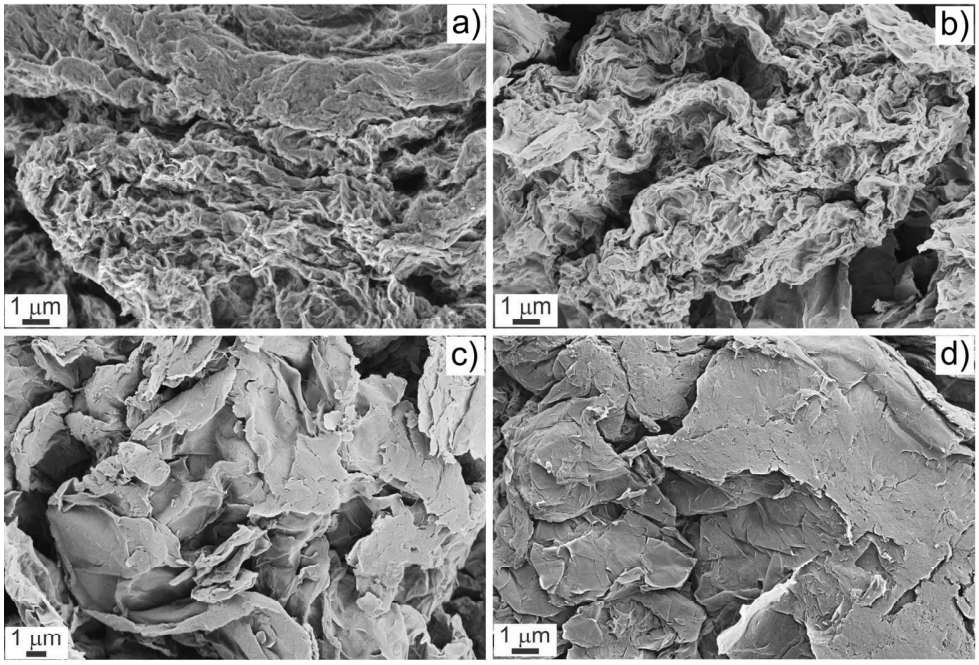

Figure 2: SEM micrographs of rGO (a), F-rGO_2 (b), F-rGO_3 (c) and F-rGO_4 (d).
140x94mm (300 x 300 DPI)

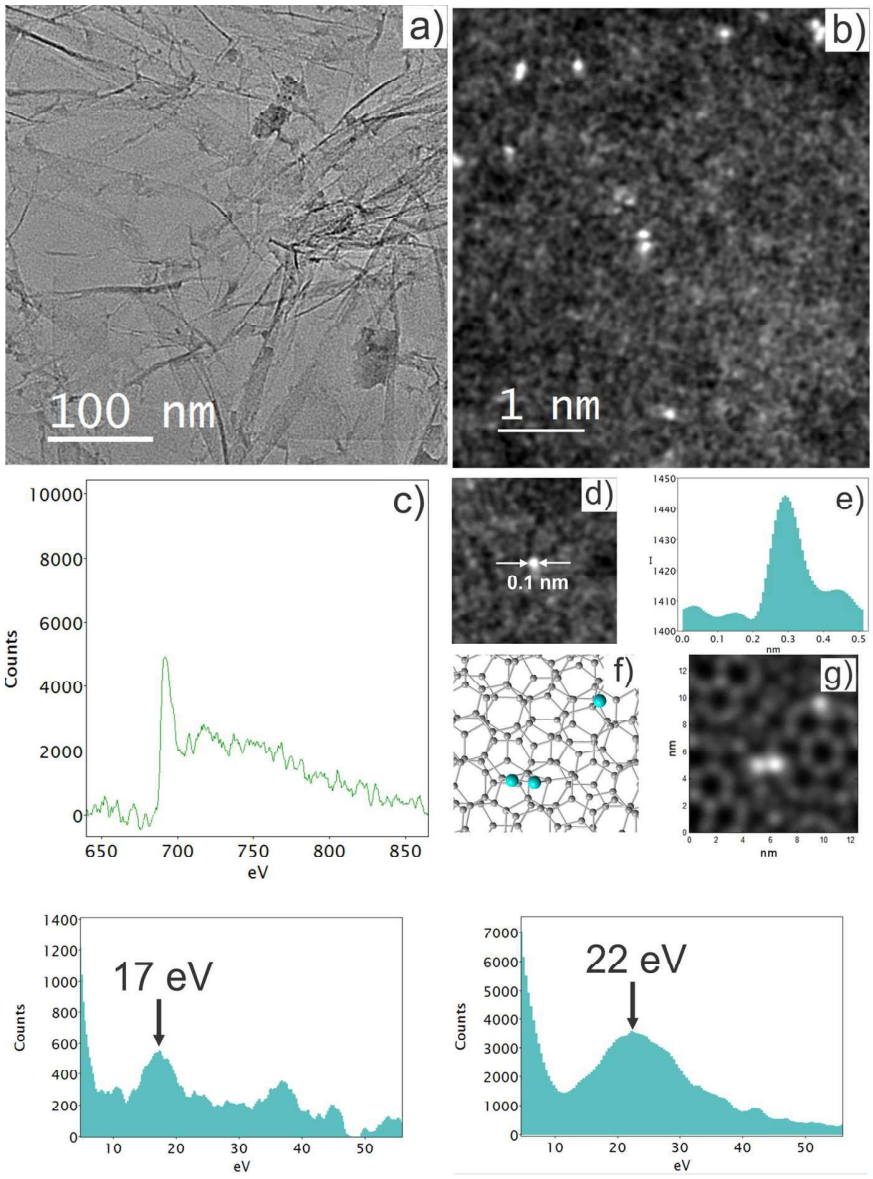

Figure 3: TEM micrograph of fluorinated graphene sheets (a). HAADF image of a thin area in the sample where individual atoms and clusters of fluorine atoms are visible (b), EELS spectrum of the area shown in Fig. 3b with characteristic fluorine K edge at 685 eV. Enlarged image of the fluorine atom (d) with the diameter (full width at half maximum) of around 0.1 nm as measured from the line profile of the intensities (e). Model of 3 layered graphene with one isolated atom and one two-atom clusters of fluorine (f) used for HAADF image calculations, shown in (g). Thickness (number of graphene layers) was estimated from the local maximum at the low loss between 12 and 30 eV as in the case of 3 – 5 layers with maximum around 17 eV (h) and 5 – 10 layers with a maximum around 22 eV (i) .
127x170mm (300 x 300 DPI)

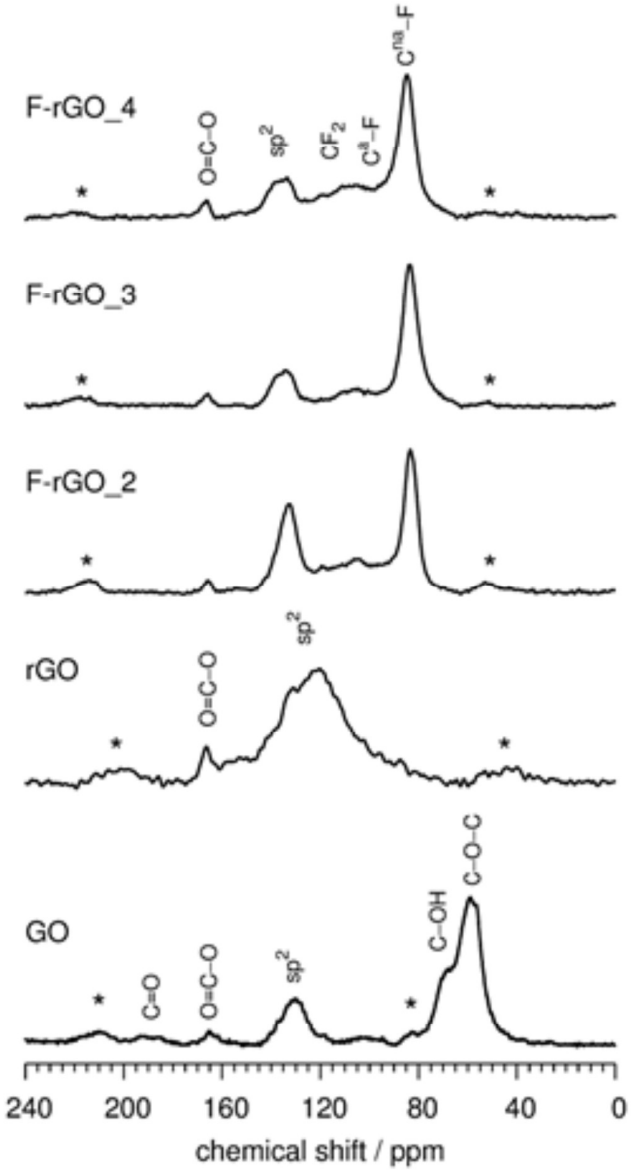

Figure 4: 13C MAS NMR spectra of materials at different stages of preparation. Asterisks denote spinning sidebands.
131x244mm (300 x 300 DPI)

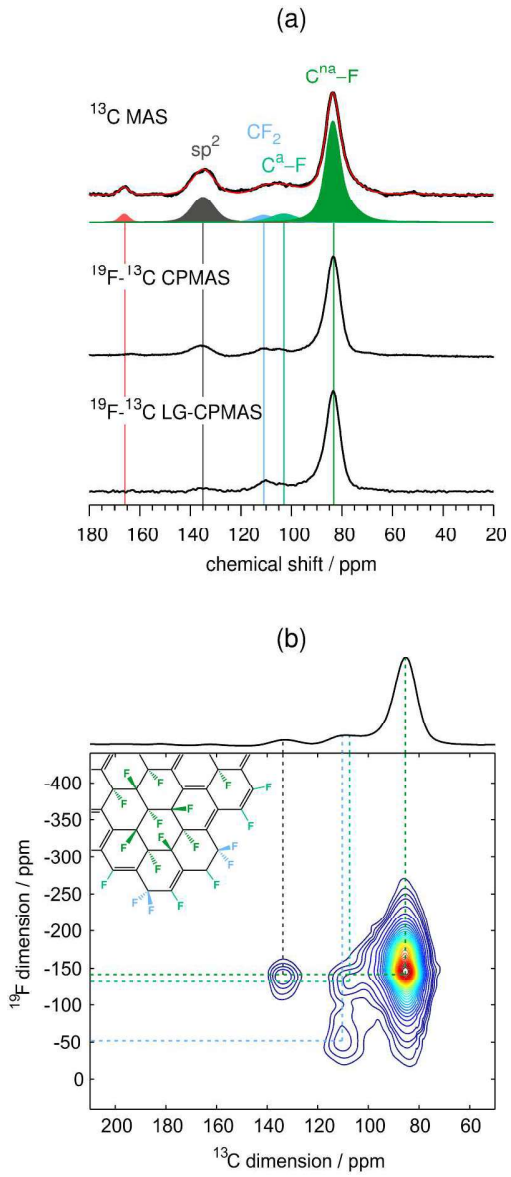

Figure 5: A more detailed NMR analysis of F-rGO_3. (a) compares13C MAS, 19F-13C CPMAS and 19F-13C LG-CPMAS NMR spectra. Vertical lines are guides for eyes and mark positions of the O=C-O, graphitic, CF2 and C-F carbon signals (with aromatic Ca and non-aromatic Cna character). Below the 13C MAS NMR spectrum, decomposition of this spectrum into individual contributions is presented. The thin red line represents the model spectrum. (b) shows 19F-13C LG-HETCOR NMR spectrum; inset shows a tentative model of the fluorinated graphene.
184x428mm (300 x 300 DPI)

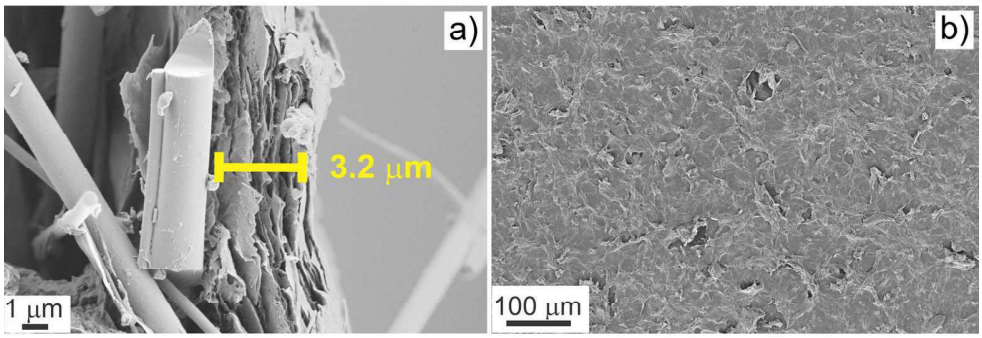

Figure 6: SEM micrograph of separator cross section showing thickness of the F-rGO_X thickness (a) and bird's eye view of the homogeneity of deposited F-rGO_X interlayer on the fiber glass separator (b).
151x109mm (300 x 300 DPI)

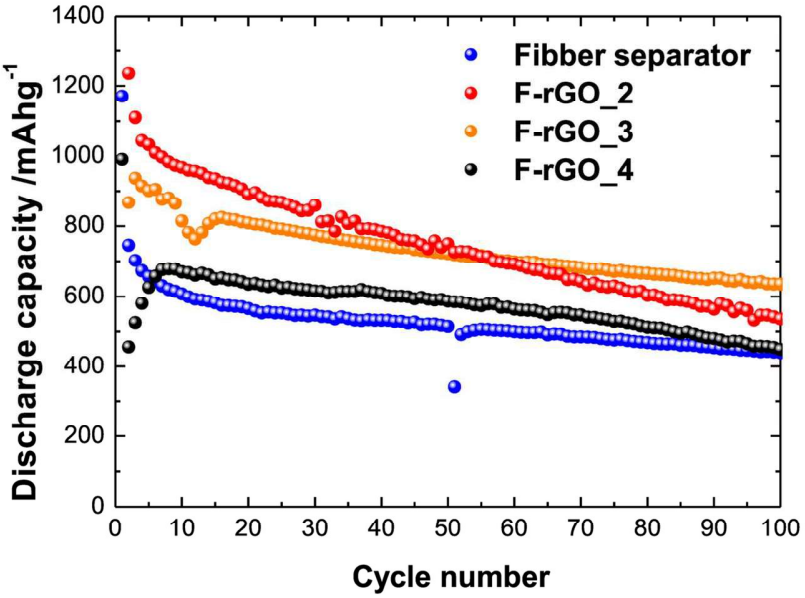

Figure 7: Cycling performance of 4 different sets of Li–S batteries (left y axis) and corresponding coloumbic efficiency (right y axis).
125x87mm (300 x 300 DPI)

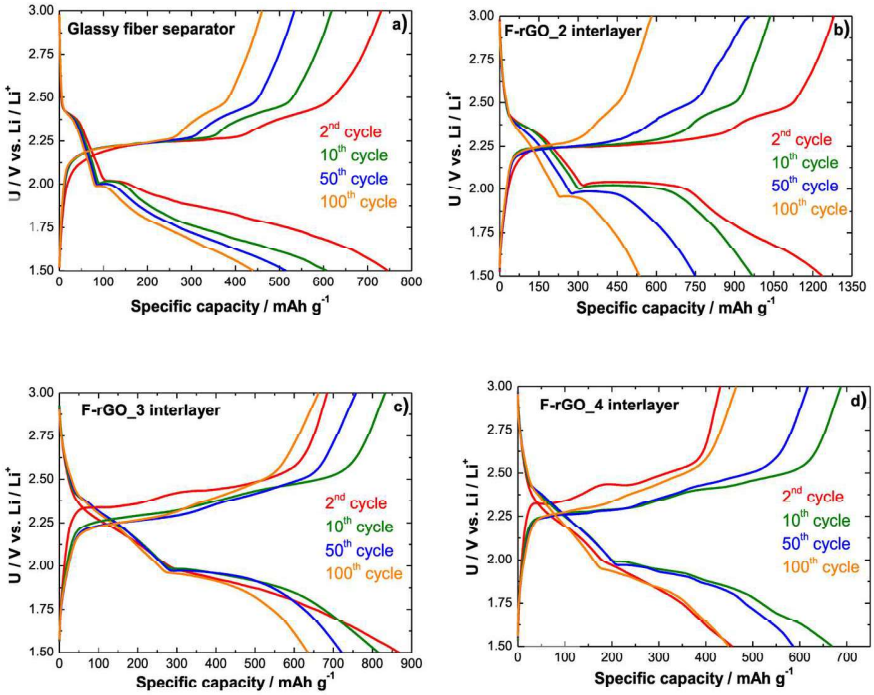

Figure 8: Galvanostatic discharge/charge curves for the 2nd, 10th, 50th and 100th cycle for a battery with a glass fiber separator (a), a separator with an F-rGO_2 interlayer (b), a separator with an F-rGO_3 interlayer (c) and a separator with an F-rGO_4 interlayer (d).
165x126mm (300 x 300 DPI)

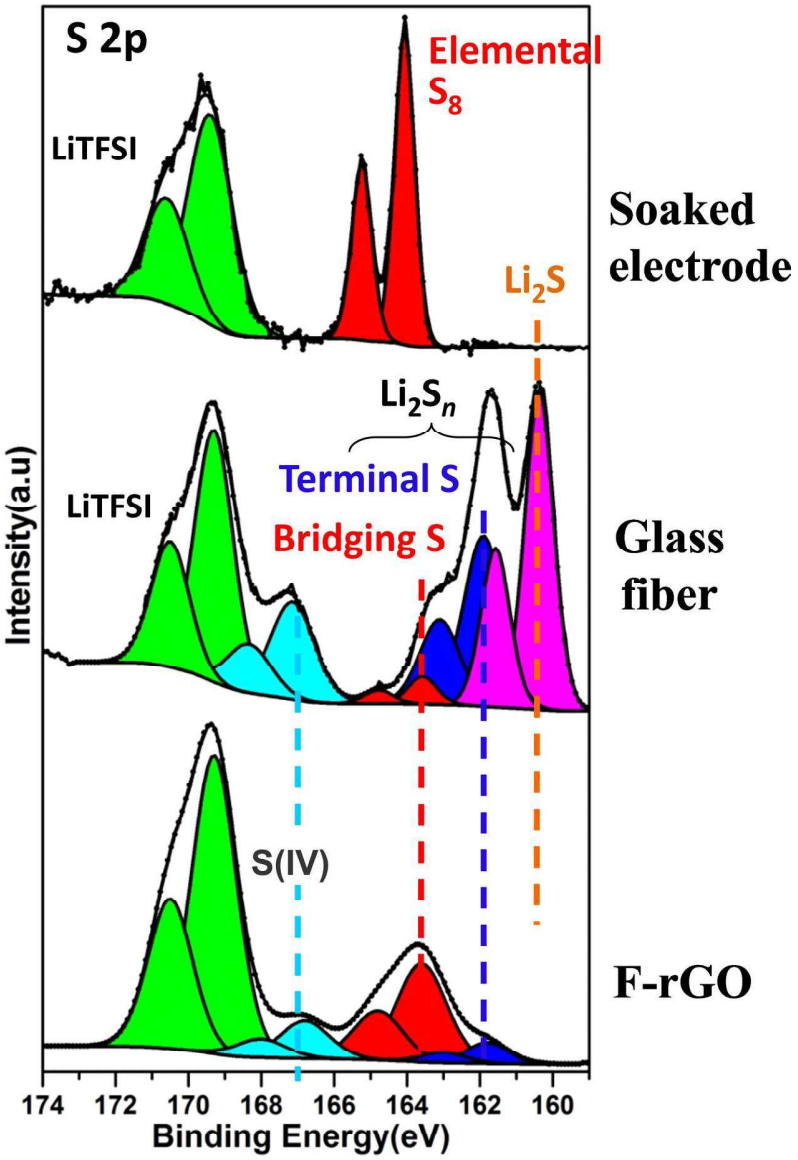

Figure 9: S 2p spectra of the composite cathode after simple contact with the electrolyte (soaked), after the first discharge with the reference glass fiber separator and with the F-rGO_3 interlayer.
166x243mm (300 x 300 DPI)

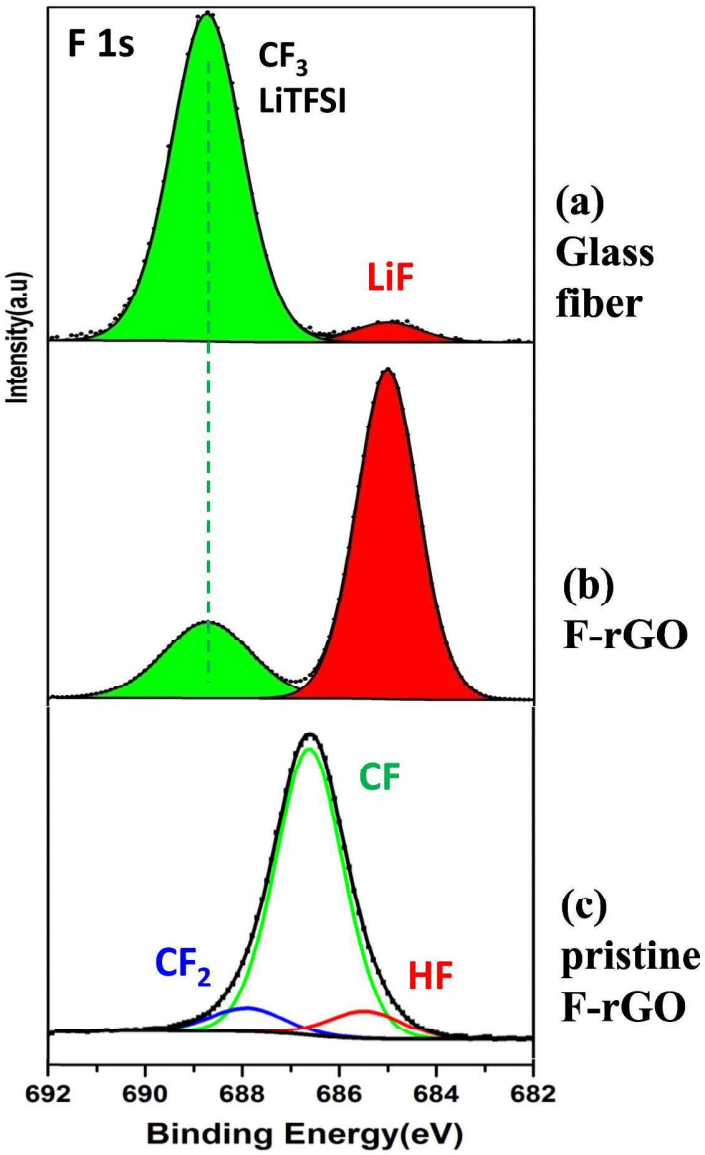

Figure 10: F 1s spectra of the separator recovered from the battery after the first discharge: reference glass fiber separator (a) and separator including the F-rGO_3 interlayer (b). Comparison with pristine F-rGO_3, as prepared by direct fluorination of rGO (c).
190x313mm (300 x 300 DPI)

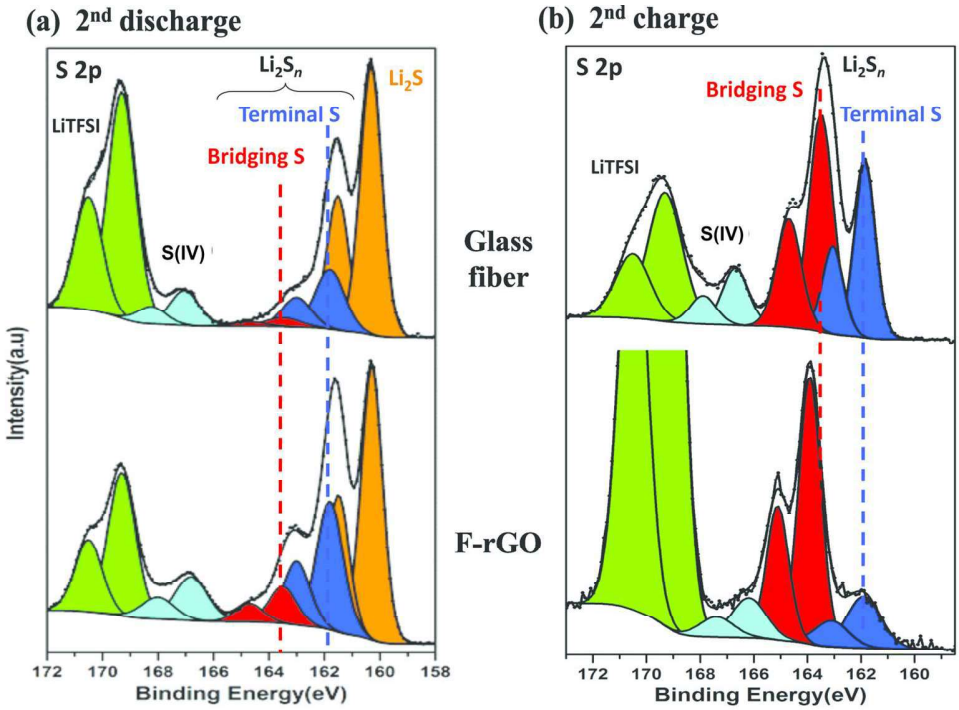

Figure 11: S 2p spectra of the composite cathode with the reference glass fiber separator and with the F-rGO_3 interlayer after the 2nd discharge (a) and after the 2nd charge (b).
143x104mm (300 x 300 DPI)

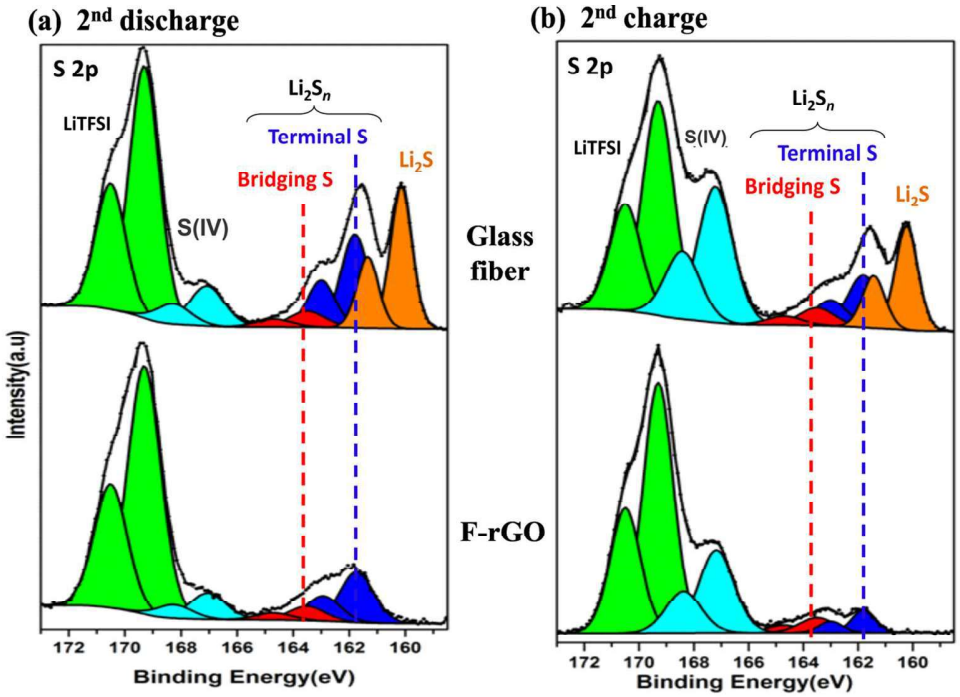

Figure 12: S 2p spectra of the lithium electrode with the reference glass fiber separator and with the F-rGO_3 interlayer after the 2nd discharge (a) and after the 2nd charge (b).
118x84mm (300 x 300 DPI)

Supplementary Information

Fluorinated Reduced Graphene Oxide as an interlayer in Li-S batteries

Alen Vizintin[a,b], Matic Lozinšek[c], Rajesh Kumar Chellappan[d], Dominique Foix[d,e], Andraz Krajnc[a], Gregor Mali[a], Goran Drazic[a], Bostjan Genorio[b], Rémi Dedryvère[d,e], Robert Dominko[*a,e]

[a] National Institute of Chemistry, Hajdrihova 19, 1000 Ljubljana, Slovenia

[b] University of Ljubljana, Faculty of Chemistry and Chemical Technology, Vecna pot 113, 1000 Ljubljana, Slovenia

[c] Department of Inorganic Chemistry and Technology, Jožef Stefan Institute, Jamova cesta 39, 1000 Ljubljana, Slovenia

[d] IPREM-ECP (UMR 5254 CNRS), University of Pau, Hélioparc, 2 av. Pierre Angot, 64053 Pau CEDEX 9, France

[e] Alistore - European Research Institute, 33 rue Saint-Leu, 80039 Amiens CEDEX, France

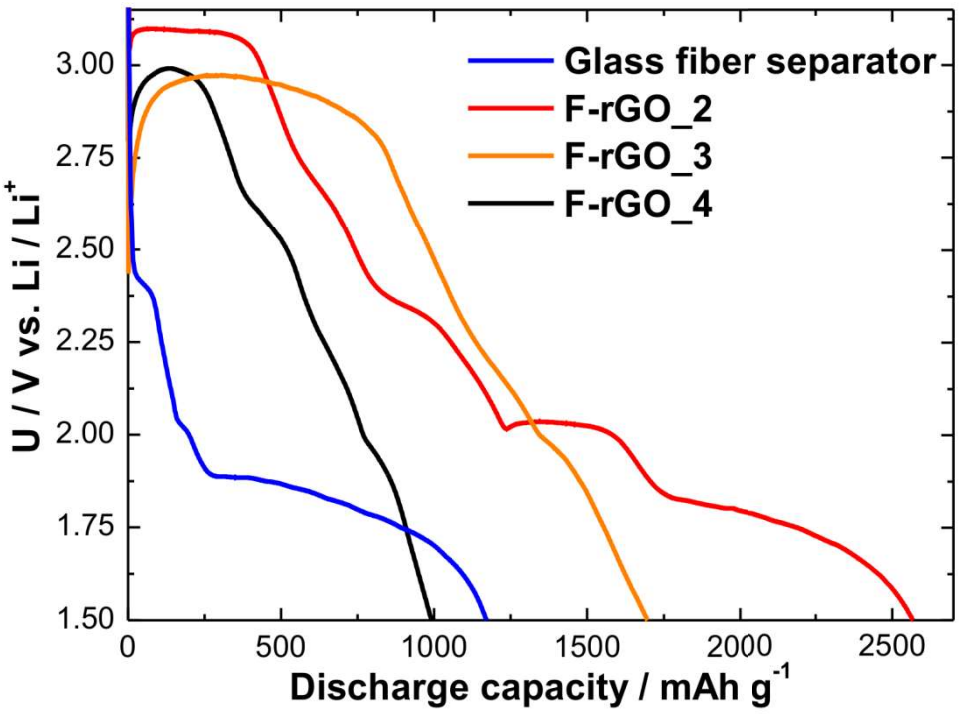

Figure S1: First discharge for 4 different sets of Li–S batteries.

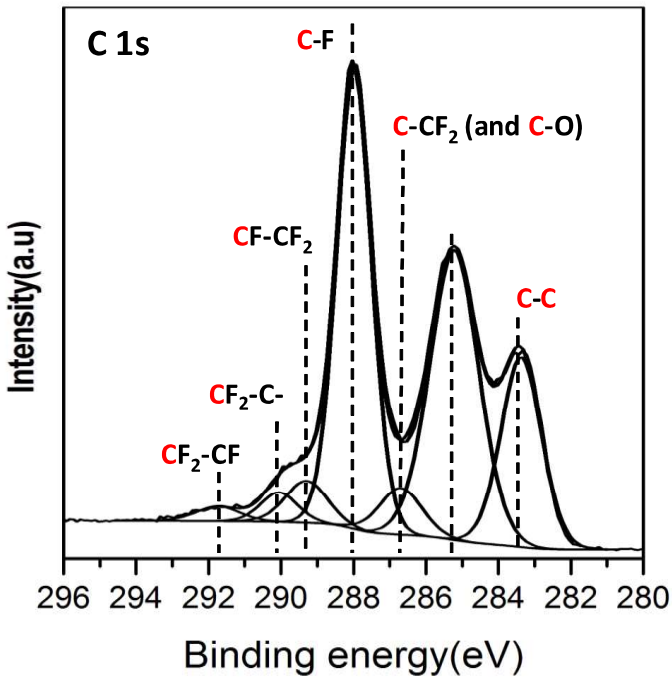

Figure S2: C 1*s* spectrum of F-rGO_3 sample